

Lagrangian Coherent Structure Analysis of Terminal Winds Detected by Lidar. Part II: Structure Evolution and Comparison with Flight Data

WENBO TANG

School of Mathematical and Statistical Sciences, Arizona State University, Tempe, Arizona

PAK WAI CHAN

Hong Kong Observatory, Hong Kong, China

GEORGE HALLER

*Department of Mechanical Engineering, and Department of Mathematics and Statistics, McGill University,
Montreal, Quebec, Canada*

(Manuscript received 19 November 2010, in final form 31 May 2011)

ABSTRACT

Using observational data from coherent Doppler light detection and ranging (lidar) systems situated at the Hong Kong International Airport (HKIA), the authors extract Lagrangian coherent structures (LCS) intersecting the flight path of landing aircraft. They study the time evolution of LCS and compare them with onboard wind shear and altitude data collected during airplane approaches. Their results show good correlation between LCS extracted from the lidar data and updrafts and downdrafts experienced by landing aircraft. Overall, LCS analysis shows promise as a robust real-time tool to detect unsteady flow structures that impact airplane traffic.

1. Introduction

This paper presents a Lagrangian analysis of low-altitude turbulent airflow structures in observational data collected at Hong Kong International Airport (HKIA). Our objective is to assess the impact of near-ground Lagrangian coherent structures (LCS) on the flight path of approaching aircraft. We favor a Lagrangian approach, as it is based on integrated quantities along fluid trajectories and hence provides a robust and objective way of locating coherent structures. By contrast, Eulerian flow features are instantaneous and *frame-dependent* indicators of coherence in unsteady velocity data.

Our methodology of LCS extraction from turbulent flows was described in Part I of this paper (Tang et al. 2011). Specifically, we applied the finite-domain finite-time Lyapunov exponent (FDFTLE) method from Tang

et al. (2010) to two-dimensional horizontal wind fields. These wind fields were obtained by processing observational data from the coherent Doppler light detection and ranging (hereinafter abbreviated as lidar) systems at HKIA using the variational retrieval technique of Chan and Shao (2007). The observational data were based on the plan position indicator (PPI) scans employed at HKIA (Tang et al. 2011). We also only use data from the lidar near the northern runway as it has a lower PPI scanning angle and the flight data were based on landings at this runway. The Lagrangian measures are advantageous as they are *frame independent* and robust with respect to localized noise in the data. Additionally, LCS analysis reveals coherent structures in more detail and with better clarity than streamline plots generated from the two-dimensional wind retrieval (Chan and Shao 2007; Tang et al. 2011). Thus, LCS analysis offers a promising platform for reliable real-time structure detection and an automated turbulence warning system for landing aircraft. The purpose of the present paper is to provide further support to this conclusion by analyzing the relation between specific LCS extracted from

Corresponding author address: Wenbo Tang, School of Mathematical and Statistical Sciences, Arizona State University, Tempe, AZ 85287.

E-mail: wenbo.tang@asu.edu

lidar data and air disturbances recorded on approaching aircraft.

Beyond the identification of aerial coherent structures, the more important question is how these coherent structures affect airplanes during takeoff and landing. One particular type of hazard of interest is high wind shear (i.e., strong headwind change over short distances) as it alters the lift force on the aircraft. Also of interest are updrafts and downdrafts as they directly exert vertical forcing on the aircraft and hence suddenly change its altitude.

We present the analysis of data collected from 20 airplane landings during the synoptic cases analyzed in Tang et al. (2011). The landing data include onboard measurements, such as horizontal wind speed and direction, vertical acceleration, and data processed by software that considers aerodynamic parameters, such as the airplane altitude and vertical wind velocity. We use these data to compare vertical and horizontal motions indicated by LCS with air disturbances experienced on board the airplane to explore the operational use of LCS in hazard detection.

The paper is outlined as follows. In section 2, we briefly review relevant Lagrangian measures for atmospheric flows. In section 3, we extract LCS from lidar data at consecutive times in two lidar datasets to study the characteristics of evolving turbulent flow structures. In section 4, we describe landing data measured on board aircraft and make comparisons with LCS. We draw conclusions and discuss open questions in section 5. Details of the two-dimensional variational wind retrieval techniques we rely on can be found in Chan and Shao (2007); detailed discussions of the lidar scanning patterns and Lagrangian measures are given in Tang et al. (2011).

2. Lagrangian coherent structures and their detection

LCS in a fluid flow are distinguished material surfaces that form the skeleton of evolving tracer patterns (Haller and Yuan 2000). Specifically, attracting LCS are material surfaces that exert locally the strongest attraction on nearby fluid trajectories and hence act as core surfaces around which the ubiquitously observed tangled filaments form in chaotic mixing experiments. By contrast, repelling LCS are the most strongly repelling material surfaces that send nearby fluid trajectories in different directions and hence are responsible for the global redistribution of matter in the flow. Although invisible in observations, repelling LCS are visible in a backward-time flow experiment.

Haller (2001) proposed that in an n -dimensional flow, repelling (attracting) LCS at time t_0 should appear as

ridges (local maximizing curves) of the forward (backward) finite-time Lyapunov exponent (FTLE) field:

$$\text{FTLE}_{t_0}^t(\mathbf{x}_0) \equiv \frac{1}{2(t-t_0)} \log \lambda_n[\mathbf{C}_{t_0}^t(\mathbf{x}_0)], \quad t > t_0, \quad (1)$$

where $\lambda_n[\mathbf{C}_{t_0}^t(\mathbf{x}_0)]$ denotes the largest eigenvalue of the Cauchy–Green strain tensor

$$\mathbf{C}_{t_0}^t(\mathbf{x}_0) \equiv \left[\frac{\partial \mathbf{x}(t; \mathbf{x}_0, t_0)}{\partial \mathbf{x}_0} \right]^T \left[\frac{\partial \mathbf{x}(t; \mathbf{x}_0, t_0)}{\partial \mathbf{x}_0} \right],$$

computed from the derivatives of current particle positions $\mathbf{x}(t; \mathbf{x}_0, t_0)$ with respect to their initial positions \mathbf{x}_0 at time t_0 . Following this proposal, Shadden et al. (2005) define LCS as FTLE ridges.

Computing FTLE from velocity fields given on small domains is challenging because a number of trajectories leave the domain quickly before FTLE ridges fully develop. A recently developed numerical algorithm, the FDFTLE method, overcomes the above problem by extending the available velocity field outside its original domain of definition without introducing spurious LCS. We employ the FDFTLE algorithm, referring the readers to Tang et al. (2010) for technical details.

Our present study is carried out on two-dimensional slices obtained from two-dimensional scans of the full three-dimensional wind velocity field. As such, the two-dimensional velocity slices may be substantially compressible. This compressibility effect may generate expansion among trajectories, leading to higher values of $\lambda_2(\mathbf{x}_0)$. To evaluate how much of the trajectory expansion comes from vertical motion in the true 3D wind data, we integrate the horizontal divergence along a trajectory $\mathbf{x}(t; \mathbf{x}_0, t_0)$ to obtain the Lagrangian divergence:

$$\text{DIV}_{t_0}^t(\mathbf{x}_0) = \frac{1}{|t-t_0|} \int_{t_0}^t \left[\frac{\partial u[\mathbf{x}(s; \mathbf{x}_0, t_0)]}{\partial x} + \frac{\partial v[\mathbf{x}(s; \mathbf{x}_0, t_0)]}{\partial y} \right] ds.$$

Positive values of $\text{DIV}_{t_0}^t(\mathbf{x}_0)$ indicate vertical convergence (divergence) in forward (backward) time. Given that the two-dimensional flow we analyze is a transverse slice of the full velocity field near the ground level, we conclude that large positive $\text{DIV}_{t_0}^t(\mathbf{x}_0)$ values (as an independent measure) indicate localized downdrafts for $t > t_0$ and updrafts for $t < t_0$.

Once an LCS is extracted as an FTLE ridge, we may also compute further Lagrangian strain and shear measures to understand the impact of the LCS on nearby trajectories in more detail. Let $\mathbf{e}_t(\mathbf{x})$ and $\mathbf{n}_t(\mathbf{x})$ denote unit tangent and normal vectors, respectively, to a one-dimensional LCS at a point \mathbf{x} and time t in

a two-dimensional flow. We use the flow map $\mathbf{F}_{t_0}^t(\mathbf{x}_0) = \mathbf{x}(t; \mathbf{x}_0, t_0)$ and define the Lagrangian measures

$$\text{STR}_\perp(\mathbf{x}_0) = \frac{1}{|t - t_0|} \ln \langle \mathbf{n}_t[\mathbf{x}(t; \mathbf{x}_0, t_0)], \nabla \mathbf{F}_{t_0}^t(\mathbf{x}_0) \mathbf{n}_{t_0}(\mathbf{x}_0) \rangle,$$

$$\text{STR}_\parallel(\mathbf{x}_0) = \frac{1}{|t - t_0|} \ln \langle \mathbf{e}_t[\mathbf{x}(t; \mathbf{x}_0, t_0)], \nabla \mathbf{F}_{t_0}^t(\mathbf{x}_0) \mathbf{e}_{t_0}(\mathbf{x}_0) \rangle,$$

and

$$\text{SHR}(\mathbf{x}_0) = \frac{1}{|t - t_0|} \ln \langle \mathbf{e}_t[\mathbf{x}(t; \mathbf{x}_0, t_0)], \nabla \mathbf{F}_{t_0}^t(\mathbf{x}_0) \mathbf{n}_{t_0}(\mathbf{x}_0) \rangle, \tag{2}$$

which quantify the strain normal to the LCS, the strain tangential to LCS, and the shear tangential to the LCS, respectively (here and below, the angle brackets indicate inner product). Specifically, in regions where STR_\perp dominates we have hyperbolic LCS since the separation is mostly transversal to the LCS, whereas in regions where SHR or STR_\parallel dominates we have shear LCS since the separation is aligned with the LCS topology. In the context of this paper, we interpolate the measures along the landing trajectory and study the Lagrangian stretching and shear rates associated with FDFTLE maxima in terms of interpreting the local flow information near LCS. For more detail on these measures, we refer the reader to Tang et al. (2011).

Recently, mathematically exact criteria for hyperbolic LCS have been developed in Haller (2011), aiming at

robust extraction of Lagrangian structures that *do* repel/attract nearby trajectories the most. The criteria provided in Haller (2011) are based on the variational theory that yields sufficient and necessary criteria for hyperbolic LCS in terms of the invariants of $\mathbf{C}_{t_0}^t(\mathbf{x}_0)$. In his paper, hyperbolic LCS is defined as material lines/surfaces where the finite-time normal repulsion rate $\rho_{t_0}^t(\mathbf{x}_0, \mathbf{n}_0)$, defined as the amount of stretching along the normal direction to the LCS, and the finite-time normal repulsion ratio $\nu_{t_0}^t(\mathbf{x}_0, \mathbf{n}_0)$, defined as the ratio between normal and tangential stretching, are both greater than 1.

To summarize the main result for our present two-dimensional context, we fix the times t_0 and t , and denote the eigenvalues of $\mathbf{C}_{t_0}^t(\mathbf{x}_0)$ by

$$0 < \lambda_1(\mathbf{x}_0) \leq \lambda_2(\mathbf{x}_0), \tag{3}$$

with the corresponding Lagrangian strain eigenvectors denoted as $\xi_1(\mathbf{x}_0)$ and $\xi_2(\mathbf{x}_0)$. We also note that FTLE ridges coincide with the ridges of the $\lambda_2(\mathbf{x}_0)$ by Eq. (1).

As proved in theorem 7 of Haller (2011), an FTLE ridge marks a hyperbolic LCS in the airflow if and only if

- 1) the FTLE ridge is pointwise normal to the largest strain eigenvector field $\xi_2(\mathbf{x}_0)$ and
- 2) the matrix

$$\mathbf{L} = \begin{pmatrix} -\frac{1}{\lambda_2^2} \langle \xi_2, \nabla^2 \lambda_2 \xi_2 \rangle + 2 \frac{\lambda_2 - \lambda_1}{\lambda_1 \lambda_2} \langle \xi_1, \nabla \xi_2 \xi_2 \rangle^2 & 2 \frac{\lambda_2 - \lambda_1}{\lambda_1 \lambda_2} \langle \xi_1, \nabla \xi_2 \xi_2 \rangle \\ 2 \frac{\lambda_2 - \lambda_1}{\lambda_1 \lambda_2} \langle \xi_1, \nabla \xi_2 \xi_2 \rangle & \frac{2\lambda_2 - \lambda_1}{\lambda_1 \lambda_2} \end{pmatrix}$$

is pointwise positive definite along the FTLE ridge.

Condition 1 is a consequence of the alignment property satisfied by hyperbolic LCS, which requires $\rho_{t_0}^t(\mathbf{x}_0, \mathbf{n}_0) > 1$ and $\nu_{t_0}^t(\mathbf{x}_0, \mathbf{n}_0) > 1$. In effect, these two measures relate to our paper as $\rho_{t_0}^t(\mathbf{x}_0, \mathbf{n}_0) = e^{\text{STR}_\perp |t-t_0|}$ and $\nu_{t_0}^t(\mathbf{x}_0, \mathbf{n}_0) = e^{\text{STR}_\perp |t-t_0|} / e^{\text{STR}_\parallel |t-t_0|}$. The extra condition (condition 2) ensures that the repelling rate is a local maxima along the direction of the largest strain, which we did not have in Tang et al. (2011). Note that no analog of SHR was given in Haller (2011). However, this measure still plays an important role in categorizing local flow topology. In this paper, the extra test of hyperbolicity allows rigorous analyses of real-time hazard detection and forecasting on the coherent structures most conducive to flow hazard for airplanes, since strong transversal strains imply strong vertical motion.

Because the exact condition (condition 1) on orthogonality is valid for large time, and our numerical

extraction scheme only covers 3 frames of data, it is relaxed by (i) the requirement that $|\langle \xi_2 \cdot \nabla \lambda_2 \rangle| < 0.175$. This condition implies that the angle between the largest strain vector and the tangent vector on the ridge is larger than 80°. Ridge points satisfying the above relaxed condition and condition 2 do repel nearby trajectories. Hyperbolic LCS satisfying 1 that repel nearby trajectories the most (where condition 1 is satisfied precisely) reside near these ridge points. For numerical accuracy of the eigenvector extraction, a circle of initial conditions is advected with a nearby ridge point and the expansion rates and directions are extracted as the Lyapunov exponents and vectors. This indeed is the celebrated bred vector method used commonly for ensemble forecasting (Toth and Kalnay 1997).

To evaluate condition 2, note that by Sylvester's theorem it is equivalent to

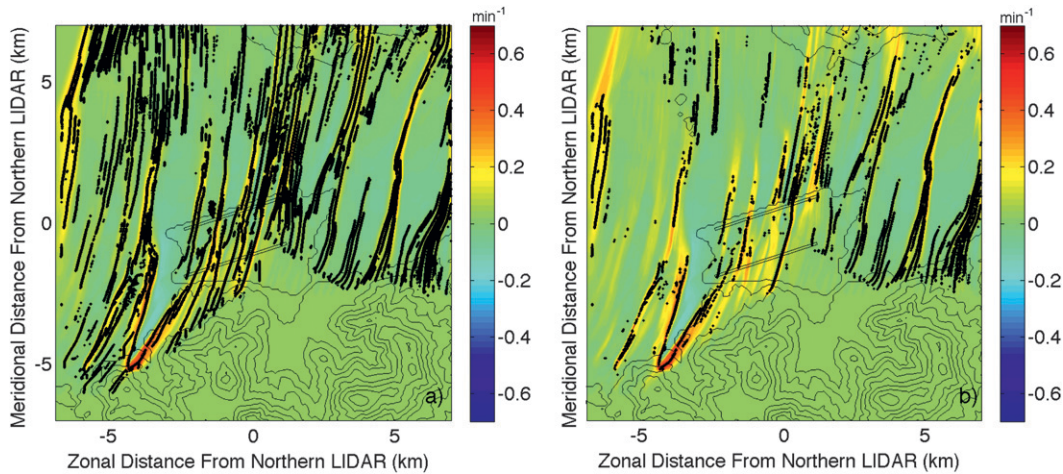


FIG. 1. Comparison between FDFTLE ridge and true hyperbolic LCS before and after the tests outlined in section 2. (a) FDFTLE ridge extracted from backward-time integration at 1436 UTC 19 Apr 2008. The black isocontours denote the HKIA terrain and runway strips. The color map is the FDFTLE field. FDFTLE ridges are shown as the collection of black dots. (b) After the hyperbolic LCS tests i and ii, we plot the portions of FDFTLE ridge that satisfy the conditions as the black dots. In general, for the data at HKIA, major ridge structures with highly distinguished FTLE values do qualify as LCS.

$$L_{11} = -\frac{1}{\lambda_2^2} \langle \xi_2, \nabla^2 \lambda_2 \xi_2 \rangle + 2 \frac{\lambda_2 - \lambda_1}{\lambda_1 \lambda_2} \langle \xi_1, \nabla \xi_2 \xi_2 \rangle^2 > 0,$$

$$\det \mathbf{L} = -\frac{2\lambda_2 - \lambda_1}{\lambda_1 \lambda_2^3} \langle \xi_2, \nabla^2 \lambda_2 \xi_2 \rangle + 2 \frac{\lambda_2 - \lambda_1}{\lambda_1 \lambda_2^2} \langle \xi_1, \nabla \xi_2 \xi_2 \rangle^2 > 0,$$
(4)

where L_{11} is the first diagonal entry of the matrix \mathbf{L} . Observe that Eq. (4) is equivalent to

$$\langle \xi_1, \nabla \xi_2 \xi_2 \rangle^2 > \frac{\langle \xi_2, \nabla^2 \lambda_2 \xi_2 \rangle}{2\lambda_2(\lambda_2 - \lambda_1)} \max(\lambda_1, 2\lambda_2 - \lambda_1)$$

$$= \frac{2\lambda_2 - \lambda_1}{2\lambda_2(\lambda_2 - \lambda_1)} \langle \xi_2, \nabla^2 \lambda_2 \xi_2 \rangle,$$

where we have used Eq. (3). Therefore, condition 2 can be reformulated as (ii) $\langle \xi_1, \nabla \xi_2 \xi_2 \rangle^2 > [(2\lambda_2 - \lambda_1)/2\lambda_2(\lambda_2 - \lambda_1)] \langle \xi_2, \nabla^2 \lambda_2 \xi_2 \rangle$.

Note that, by definition, on a second-derivative FTLE ridge with unit normal \mathbf{n} , we have $\langle \mathbf{n}, \nabla^2 \lambda_2 \mathbf{n} \rangle < 0$. As a result, if the ridge's normal is close enough to ξ_2 , then ii is satisfied. Therefore, for a second-derivative FTLE ridge, conditions i and ii both provide bounds on the difference between the ridge normal $\mathbf{n} \perp \nabla \lambda_2$ and the larger strain eigenvector ξ_2 .

Studying the datasets at HKIA, we find that even though a significant number of FDFTLE ridge points, defined from the “second derivative ridge” (Shadden et al. 2005) are removed by the hyperbolicity test, the cores of the strongest highlighters do still qualify as hyperbolic LCS, that is, satisfy conditions i and ii. To

illustrate this, we plot in Fig. 1 a comparison between FDFTLE ridges extracted using techniques outlined in Mathur et al. (2007) and the portion of the ridge that qualifies as hyperbolic LCS, for a randomly chosen case at 1436 UTC 19 April 2008. The comparison is carried out for a backward-time integration. Shown in both panels of Fig. 1, the color maps are the same FDFTLE fields. HKIA topography and the runway strips are also plotted for reference. The black dots in Fig. 1a are exactly on FDFTLE ridges. The portions of the extracted FDFTLE ridges that satisfy conditions i and ii are plotted in Fig. 1b. As seen in this plot, the major structures are still hyperbolic. In the following sections, our analyses will be based on ridge extraction from the FDFTLE fields and comparisons with the additional test of conditions i and ii.

3. Coherent structure evolution

In Tang et al. (2011), we discussed how to extract and infer flow structures from Lagrangian measures Eq. (2), using examples from three different episodes of synoptic flows between April 2008 and February 2009. In this section, we study the evolution of these flow structures from two episodes and obtain a dynamical picture of the coherent structures. August 2008 data are omitted because of lack of quality data over time for structure evolution. Structure evolution is important for flight data analysis, since we are interested in how LCS change in shape and location and affect the last few minutes of airplane approaches.

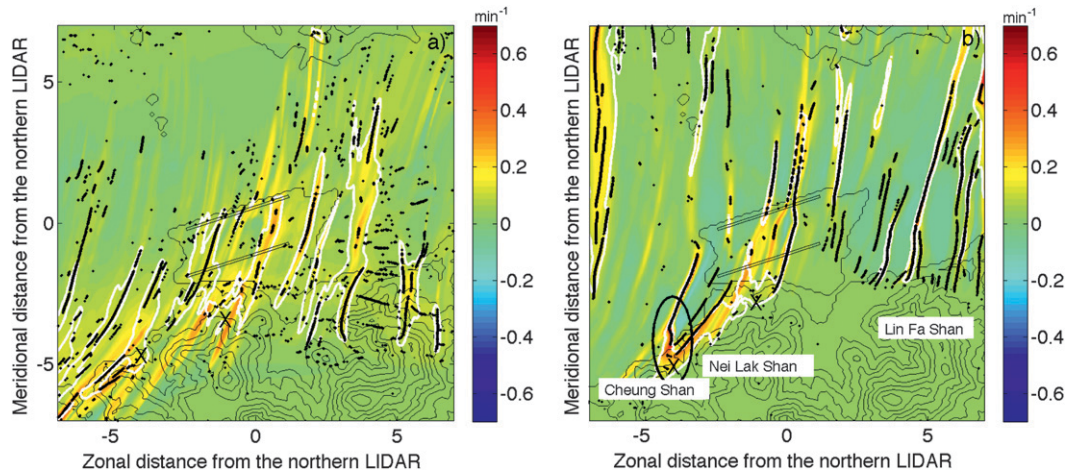


FIG. 2. LCS obtained at 1441 UTC 19 Apr 2008. (a) Forward-time FDFTL field. Red regions indicate repelling structures. The white isocontours correspond to DIV with value of 0.09. (b) Backward-time FDFTL field. Red regions indicate attracting structures. The white isocontours correspond to DIV with value 0.06. Black points indicate FDFTL ridges passing the hyperbolic LCS tests. Hairpin structures next to mountain peaks and FDFTL ridges are marked by Xs. Black ellipse in (b) indicates a region of structure shedding.

LCS are extracted as ridges of the FDFTL field, at 150-s intervals. The Lagrangian horizontal divergence (DIV), shear (SHR), and strains normal and parallel to the LCS (STR_{\perp} and STR_{\parallel}) are also computed to categorize the type of motion each LCS exhibits. We further compute the maximal repelling conditions i and ii outlined in section 2 for comparison. We briefly recall that the April 2008 case corresponds to a southwesterly flow in a stable boundary layer and the February 2009 case corresponds to an easterly flow in a stable boundary layer. Contrasts among the synoptic conditions can be found in Tang et al. (2011).

a. Structure shedding

A common feature for both episodes of synoptic flows is the presence of strong winds near the airport. This results in the generation and shedding of coherent turbulent structures when large-scale flows climb over topography and break. For example, in Fig. 6 of Tang et al. (2011), we infer from the Lagrangian measures that a couple of hairpin structures exist downwind of mountain peaks on Lantau Island on 19 April 2008, during the spring tropical cyclone. In fact, extraction of LCS at different times indicates that these structures periodically shed small patches of velocity anomalies, which are subsequently advected downwind. One such shedding-generation event is captured between 1436–1446 UTC.

To aid discussion, we show in Fig. 2 the overall conditions of coherent structures at 1441 UTC 19 April 2008. This corresponds to the time when a hairpin structure detached from the topography at the lower-left corner of the domain, downwind of mountain peak Cheung Shan.

In this figure, black isocontours are the topography shown at 100-m intervals. The airport island is located at the center of the panels and the two slender rectangles are the runway strips. The color maps are the FDFTL fields extracted from forward-time (Fig. 2a) and backward-time (Fig. 2b) trajectories. Ridges of FDFTL are in red, corresponding to the largest fluid trajectory separation over time. Superimposed in the plots are the white DIV isocontours at 90th percentile (values in the caption), showing strong vertical motions. In general vertical motions, appearing as updrafts and downdrafts, are associated with the LCS. Also shown in black points are the sections of the FDFTL ridges that pass the LCS tests i and ii. As seen, the most significant forward-time ridge and most of the backward-time ridge survive the tests and do organize hyperbolic motion. In terms of physical structures, a couple of hairpins can be identified near the Xs marked at the corresponding mountain peaks. The shape of the left hairpin is undergoing strong deformation and is associated with structure shedding. This hairpin is highlighted in the black ellipse in Fig. 2b.

Figure 3 shows the evolution of the velocity structure during the shedding-generation event on 19 April 2008. In particular, we compare the line-of-sight (LOS) velocities and the backward-time FDFTL fields. Figures 3a–d show the LOS velocities at 150-s intervals, between 1436 and 1444 UTC. Figures 3f–i show the backward-time FDFTL at the same time, superimposed with white isocontours of DIV and attracting LCS points surviving conditions i and ii. Note that since the LOS velocity is a measure of radial velocity toward/from the lidar, there is inherently a radial pattern of the measurements even if

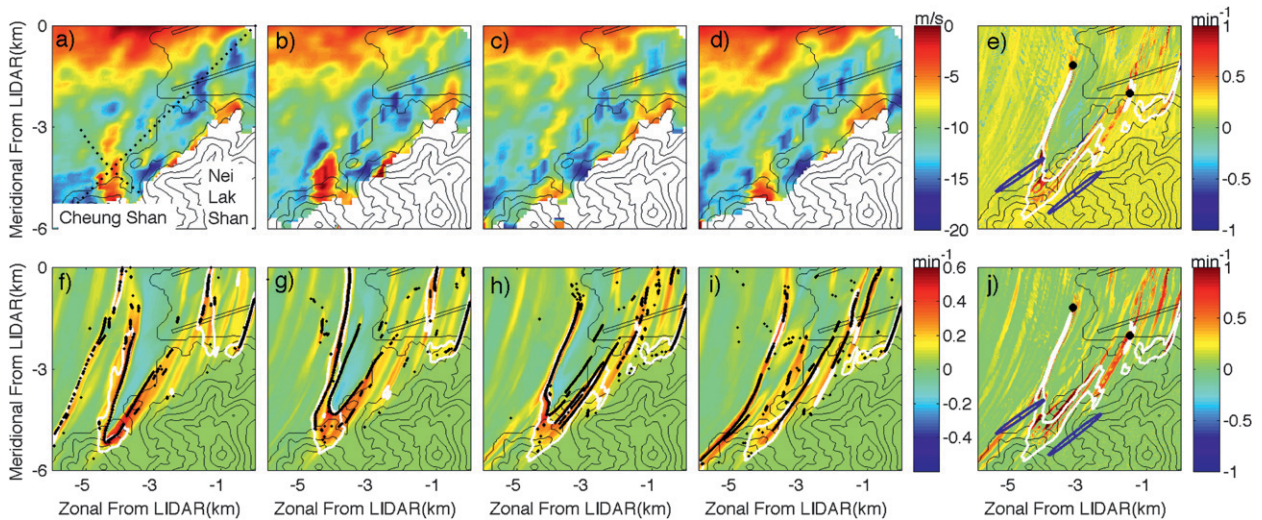


FIG. 3. LOS velocity from lidar and the backward-time FDFTLE associated with the retrieved wind fields at five different times. Columns from left to right: 1436–1444 UTC 19 Apr 2008, with 150-s intervals. (a)–(d) The LOS velocity; (f)–(i) FDFTLE. In (f)–(i), the white isocontours correspond to DIV with value 0.09. Black points indicate FDFTLE ridges passing the hyperbolic LCS tests. The black dots in (a) indicate the coverage of azimuthal angles and radial distances in Hovmöller diagrams in Fig. 4. (e) Backward-time SHR at 1441 UTC; (j) backward-time STR_{\perp} at 1441 UTC. The white isocontours ($DIV = 0.09$) are shown in both (e) and (j). The two black dots are initial conditions passing the hyperbolicity tests. The two blue ellipses with centered dots show the evolution (5 min in backward time, with exaggeration) of a circle of points initially uniform distance away from each of the black points and the evolution of the black points themselves.

the measured velocity is uniform in direction and magnitude. Since the velocity has radial heterogeneity, we use LOS directly for analyses. We will use LOS “perturbation” in a later event to try to distinguish patterns not aligned with lidar.

The start of the shedding indeed appeared as the coalescence of two nearby patches of velocity anomalies. At 1436 UTC, these two patches are found downwind of Cheung Shan (Fig. 3a). The smaller patch on the left is seen next to the hairpin as a weak attractor near $(-4.5 \text{ km}, -4.5 \text{ km})$ in Fig. 3f. At 1439 UTC, in Fig. 3b, the velocity anomalies coalesce and appear as just a single patch. The backward-time FDFTLE in Fig. 3g clearly indicates that this single patch is due to the two anomalies merging. At 1441 UTC, the two patches merge completely and leave the topography (Fig. 3c). They also appear to lose strength as they are advected with the background flow. The backward-time FDFTLE in Fig. 3h shows that the merged structure is advected downwind, giving way to newly emerged flow structures. The new patch, appearing as a weak velocity anomaly, is seen in Fig. 3c, immediately downwind of Cheung Shan. It is yet too weak to be picked up as an organizing structure in Fig. 3h. Later, in Fig. 3d, we find that the detached structure quickly disappears after shedding off and the weak anomaly started in Fig. 3c has now grown stronger. In Fig. 3i, we see that this patch of reverse flow becomes a dominant structure trailing Cheung Shan again.

In addition to FDFTLE, we show SHR in Fig 3e and STR_{\perp} in Fig. 3j computed at 1441 UTC, superimposed with DIV isocontours and topographic features. Both measures show relatively strong values near the FDFTLE ridge, but the measure STR_{\perp} appears to be stronger than SHR. It can also be inferred that in general, on the FDFTLE ridge, $STR_{\perp} > STR_{\parallel}$, since most of the ridge points survive the hyperbolic LCS tests. To aid visualization of behavior of fluid trajectories, we consider two ridge points passing the tests i and ii. The locations for these two points are marked by the two black dots in Figs. 3e,j. We examine the evolution of these two points along with two circles of nearby initial conditions 1 mm away from the ridge points. This distance is sufficiently small to capture the local linear behavior of the flow. The end positions of the two ridge points and the nearby circles are shown as blue dots, with exaggeration so the evolution is visible. Not much of tangential stretching is seen, yet significant stretching and tilting are found near these points. We hence infer the flow structures to be strong updraft and shear, but weak tangential dilation.

Hovmöller diagrams are useful to identify the time evolution of structures at certain spatial positions. Since we are concerned with the evolution of extracted flow structures, it is natural to use the Hovmöller diagram to identify flow features revealed in the LOS velocity for comparison. Henceforth, in addition to extracting LCS, we plot Hovmöller diagrams to compare shedding flow

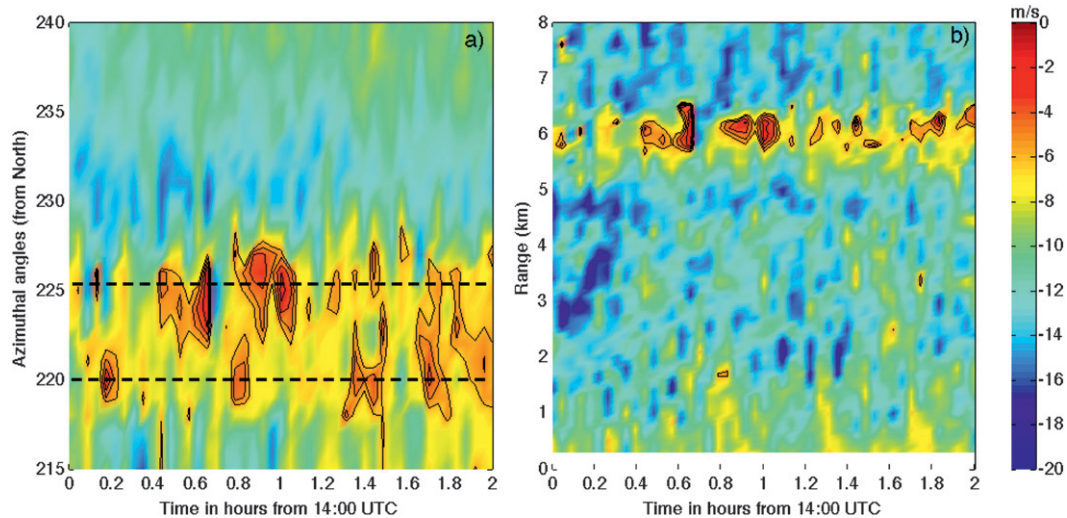


FIG. 4. Hovmöller diagram taken with the 1.4° lidar scan between 1400 and 1600 UTC 19 Apr 2008. (a) Azimuthal angles from 215° to 240° at range 6 km from the lidar. The two dashed lines correspond to azimuthal angles where structure shedding is found. (b) Azimuthal angle of 225° for different ranges from the lidar. The Hovmöller diagram coverage is revealed in Fig. 3a.

structures against similar tropical cyclone cases in previous studies. Figure 4 shows these diagrams between 1400 and 1600 UTC. In Fig. 4a, the LOS velocity is shown between the 215° azimuth and 240° azimuth, in 1° intervals, at 6-km range from the lidar. The azimuthal angles are determined from due north and in clockwise directions. Their locations are marked by the arc of black dots in Fig. 3a. There are two streaks of velocity bubbles indicating reversal flows near 220° and 225° azimuth (marked by the two dashed lines). The size of the bubbles is on the scale of several hundred meters, and the shedding period is usually around 0.4 h, but can be as long as 0.6 h and as short as 0.3 h (cf. the black isocontours highlighting velocity bubbles). The region between 220° and 225° azimuth is downwind of Cheung Shan. These characteristics agree with the recirculation vortices observed in Shun et al. (2003). The observed shedding period also falls in the range of 15–45 min for structure shedding in stable boundary layer conditions near HKIA, as discussed in Chan and Shun (2005).

In addition, we plot the Hovmöller diagram at different ranges from the lidar for a fixed angle of 225° in Fig. 4b. The locations of the ranges are shown as the line of black dots in Fig. 3a. The strongest anomaly is observed at 6 km from the lidar, but we are unable to determine the speed of the recirculating bubbles from the time series. This is probably due to the following reasons: structure shedding not perfectly aligned with the lidar, coarse scanning frequency, and a quick loss of coherence as the vortices detach from the topography. As an alternative approach, we use the radiosonde

measurements based at King's Park near HKIA (Tang et al. 2011) to estimate the speed of the background flow. At 1.4° elevation and 6-km distance, the scans are roughly at 150 m MSL. The radius of Cheung Shan is roughly 2 km at this elevation and the radiosonde velocity is around 6 m s^{-1} . This leads to an estimate of the Strouhal number based on Atkinson (1981), $St = Df/U_0 \approx 0.1543\text{--}0.3086$, using the two limiting shedding periods [$D = 2000 \text{ m}$, $U_0 = 6 \text{ m s}^{-1}$, $f = (36\text{--}18 \text{ min})^{-1}$]. This estimate is within the range of 0.15–0.32 for von Kármán vortex shedding downstream of isolated islands.

We show another shedding event captured on 0115 UTC 21 February 2009, in Fig. 5. This case has very similar synoptic conditions as those shown in Chan and Shun (2005) and the shedding processes are quite alike. In this figure, Figs. 5a–d are the radial velocity measured by lidar and Figs. 5f–i show forward-time FDFTLE with white DIV isocontour and repelling LCS as black points. The structures are plotted between 0111 and 0118 UTC, at 150-s intervals. The black ellipses in Figs. 5b–d and 5g–i indicate the shedding of velocity structures. The event is located downwind of a mountain peak named Lo Fu Tau on Lantau Island. As indicated in the top panels, there is a persistent low-speed patch (toward the lidar) trailing Lo Fu Tau.

The low-speed patch embedded in high-speed background flow indicates a locally diverging structure (as fluid trajectories at the edges of the low-speed patch experience strong separation due to the velocity difference). In Fig. 5a, no shedding is yet present. Starting from Fig. 5b, at 0113 UTC, a small patch of low-speed

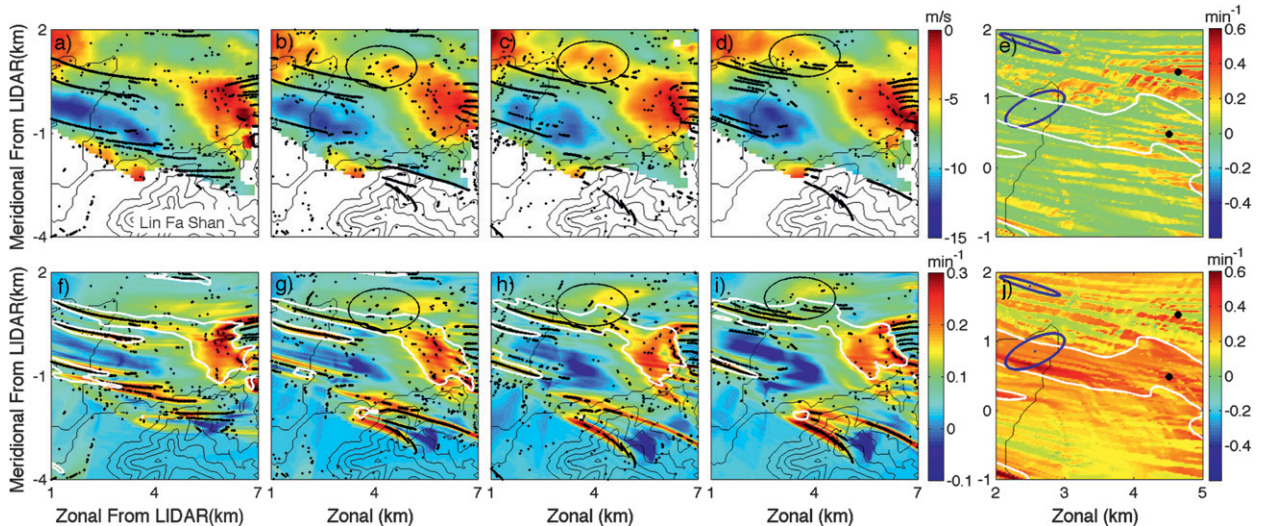


FIG. 5. Structure shedding to the east of HKIA at 0115 UTC 21 Feb 2009. (a)–(d) Lidar LOS velocities; (f)–(i) forward-time FDFTLE fields. In (a)–(d), the white isocontours correspond to DIV with value 0.09. Black points indicate FDFTLE ridges passing the hyperbolic LCS tests. The event is shown at 150-s intervals, from left to right, between 0111 and 0118 UTC. Shedding structure is located inside the ellipses. (e) SHR and (j) STR_{\perp} at 0115 UTC. The white isocontours are DIV = 0.09. The two black dots are test points on two FDFTLE ridges on the two sides of the velocity anomaly. The two blue rings of points mark the final positions of initial conditions having uniform distance from the black dots. Their evolution indicates the shearing and repelling motion of the two ridges.

flow detaches from the bigger patch and moves downwind in Figs. 5c,d. Finally, in Fig. 5d the patch merges with the red structure downwind. In Fig. 5f, we indeed find two patches of local FDFTLE maxima bounding the edge of the anomaly, marking strong separation in the following 5 min (integration time). In Fig. 5g, this patch begins to detach from the major slow-speed structure. As time progresses, the patch detaches, moves downwind, and weakens in Fig. 5i, at 0118 UTC. Using the conditions i and ii, we find that the northern bounding patch does not repel and thus does not qualify as hyperbolic LCS, whereas the southern patch does.

To aid our interpretation, we again use advection of a ring of initial conditions of distance 1 mm from two ridge points released at 0115 UTC. The color contours in Figs. 5e and 5j show SHR and STR_{\perp} at 0115 UTC, respectively. White DIV isocontours are also shown. The two ridge points we examined are shown as the scattered black dots in both panels. The northern point is chosen to be a ridge point *not* passing hyperbolicity tests whereas the southern point is chosen to be one passing the test. Clearly, the northern dot is situated in a region of high SHR and low STR_{\perp} , whereas the southern dot is in a region of low SHR and high STR_{\perp} . The final positions of these two ridge points and the associated rings of nearby trajectories are shown in blue with exaggeration. From these two panels, we infer that to the southern flank of the low-speed patch there is strong repelling motion, whereas in the northern flank, the patch experiences high shear and tangential stretching.

b. Evolution of LCS updrafts

Important LCS relevant to our analysis are not limited to the generation and shedding events. As depicted in Fig. 2b, a long and distinct ridge of updraft is persistent as an organizing structure. We show the evolution of this updraft between 1436 and 1441 UTC 19 April 2008 in Fig. 6, at 150-s intervals. This ridge of updraft originates downwind of Lin Fa Shan. The ridge could correspond to the expansion of gap flows on the two flanks of the mountain peak, leading to convergence and updraft when they meet. Unlike other coherent structures, which are localized and/or short lived, this ridge is larger in scale and stays longer in time. More important, this ridge is transversal to the runway corridor, where many flights pass through.

In the top panels of Fig. 6, we try to explore structures that would arise from examination of the LOS velocity. As mentioned earlier, the LOS velocity has inherent radial patterns. To highlight the variations from this radial pattern to discern structures not aligned with the light beam, we assume a uniform background flow in direction and magnitude best fitting the measurements, and we obtain the perturbation of LOS velocity from the difference between the measured LOS and the LOS of the uniform background, shown in Figs. 6a–c.

From these plots we can have some hint of structures emanating from the base of the mountains and possibly extending toward the northeast of the plot. On the other

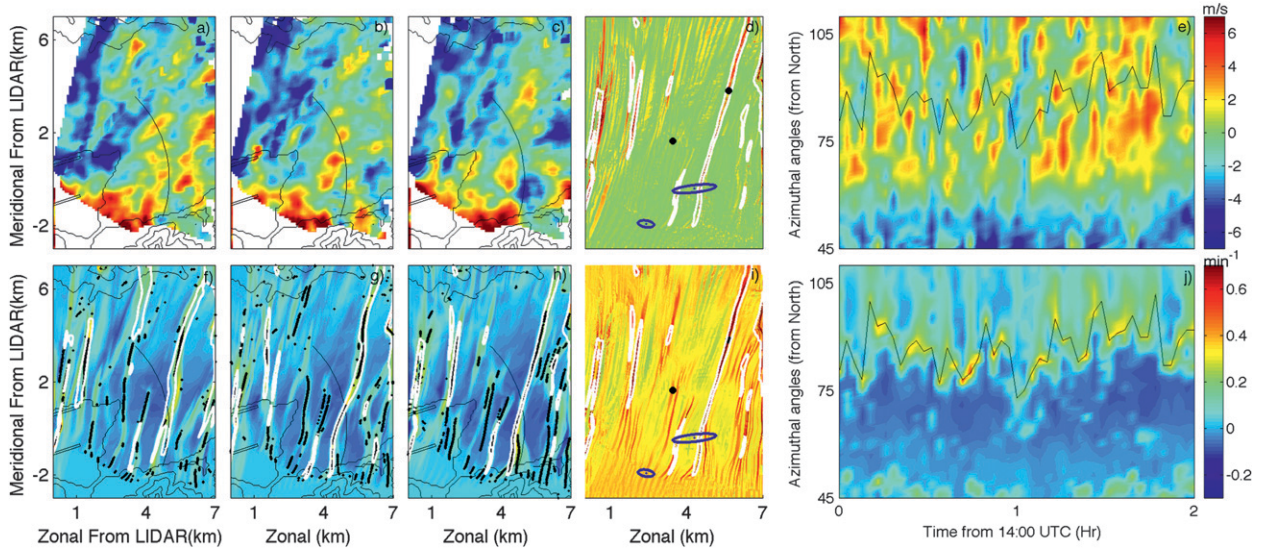


FIG. 6. Ridge of updraft identified to the east of the airport on 19 Apr 2008. (a)–(c) The LOS velocity perturbations. (f)–(h) The backward-time FDFTLLE. In these panels, the white isocontours correspond to DIV with value 0.09. Black points indicate FDFTLLE ridges passing the hyperbolic LCS tests. The different times, from left to right for each pair of plots, are 1436, 1439, and 1441 UTC. (d) SHR at 1441 UTC. (i) STR_{\perp} at 1441 UTC. The black dots and blue ellipses mark evolution of two initial conditions and nearby points on hyperbolic LCS. Color axis in (d) is the same as the bottom panels. (e) Hovmöller diagram of the LOS velocity perturbation at 5-km range between 1400 and 1600 UTC. The coverage is shown as the arc of black dots in (a). (j) Hovmöller diagram of the backward-time FDFTLLE between 1400 and 1600 UTC. The FDFTLLE maxima (on the persistent ridge) are connected by the black curve. This curve is also plotted in (e).

hand, the FDFTLLE plots, along with DIV isocontours and hyperbolic ridge points, in Figs. 6f–h do reveal the updraft structure in clarity. Similar to the shedding cases, we plot SHR in Fig. 6d and STR_{\perp} in Fig. 6i along with DIV isocontours. Two initial conditions on the ridge passing the hyperbolicity tests with nearby conditions are again plotted to aid interpretation. In this case, most of the separation can be associated with STR_{\perp} for both ridge points. In addition, we compare the Hovmöller diagram of the LOS perturbation (Fig. 6e) and the backward-time FDFTLLE (Fig. 6j) at 5-km range between 45° and 105° azimuth and 1400–1600 UTC. The black arcs in Figs. 6a–c, f–h show the location where the Hovmöller diagram is generated. Since the updraft structure is transversal to the arc 5 km from lidar, we locate its time evolution in terms of the change in azimuthal angles on the Hovmöller diagram where the ridge appears. We highlight the change in the azimuthal angle where the ridge appears in black in both Hovmöller diagrams. Again, LCS analyses reveal the pattern that is hard to discern from LOS velocity (perturbation).

On 21 February 2009 we observe a similar ridge of updraft originating downwind Lin Fa Shan, which lasts for a long time. Figure 7 shows the persisting ridge between 0349 and 0356 UTC. Figures 7a–d show lidar radial velocity at 150-s intervals. Figures 7f–i are the Lagrangian strain perpendicular to the LCS STR_{\perp} computed from

the backward-time trajectories, associated with white DIV isocontours and attracting LCS. STR_{\perp} is used to illustrate the attracting nature of the ridge. Trajectories transversal to the ridge approach the ridge because of strong negative strain. It is seen that the measure STR_{\perp} aligns very well with the hyperbolic test, indicating that the trajectories near these ridges are truly experiencing strong attraction. As a comparison, we show SHR and STR_{\parallel} in Figs. 7e and 7j, respectively, along with DIV isocontours and the evolution of initial conditions passing hyperbolicity tests. We again see clear indication of normal stretching. Since the structure is transversal to runway strips, large STR_{\perp} also indicate sudden headwind changes. The perpendicular strain and the associated updraft may affect aircraft landings from the west in easterly wind situations. As such, this ridge could also have significant implications for aircraft operation with regard to wind shear and turbulence.

4. Airplane-landing studies

During the spring tropical cyclone and spring easterly episodes, data from 20 airplane landings were made available to study the interaction between the turbulent flow structures and airplane motions. Among these landings, several flights missed the approach and landed successfully later. We present two of such cases in this

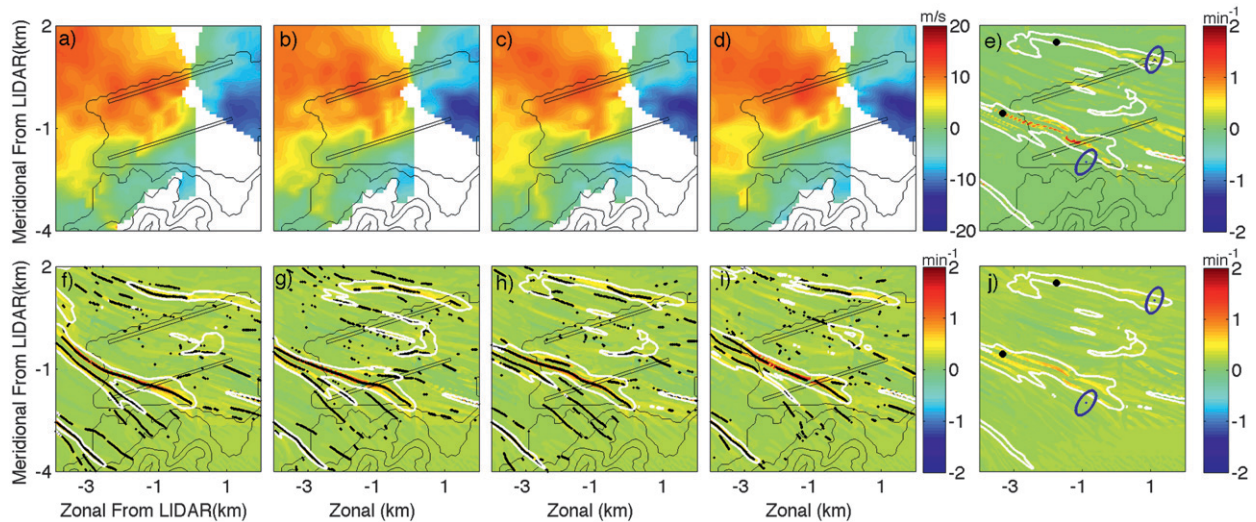


FIG. 7. Persisting ridge of updraft originating downwind Lin Fa Shan between 0349 and 0356 UTC 21 Feb 2009. (a)–(d) The lidar radial velocity; (f)–(i) the Lagrangian strain STR_{\perp} perpendicular to the LCS. In these panels, the white isocontours correspond to DIV with value 0.09. Black points indicate FDFTLT ridges passing the hyperbolic LCS tests. From left to right, for each column, the time intervals are 150 s. (e) SHR at 0354 UTC; (j) STR_{\parallel} at 0354 UTC. White DIV isocontours are superimposed and evolutions of two initial conditions (black points) passing the hyperbolicity tests are illustrated as the blue ellipses.

section, each containing one unsuccessful and one successful landing. We also discuss the overall performance of LCS analysis. The airplanes experienced wind shear or turbulence in different magnitudes during their approaches. However, whether the missed-approach decision was made because of any particular disturbance or because of turbulence at all is unknown.

The four landings were conducted at 1346 and 1414 UTC 19 April 2008 from 25R (the northern runway approaching from the east) and at 0837 and 0902 UTC 21 February 2009 from 07L (the northern runway approaching from the west). We present in Figs. 8–11 the respective analyses of LCS with each individual landing record. Each of these figures is prepared with the same layout and thus we start our explanation from Fig. 8, which denotes the missed approach at 1346 UTC 19 April 2008.

In Figs. 8a and 8b, we superimpose the aircraft trajectory with the HKIA topography and the FDFTLT fields extracted at the time when the aircraft reaches the runway threshold (1346 UTC). The black isocontours indicate nearby topography. The color maps show forward-time and backward-time FDFTLT, respectively. The white isocontours signify major structures from DIV, indicating strong vertical motion. As seen, these structures mostly align with FDFTLT maxima. The thick white line in the southwest corner of the domain is the northern runway strip. The black dot at (0, 0) shows the location of the northern lidar. The aircraft-landing trajectory from the east is shown as the thin black line

aligned with the runway strips. We see that several terrain-induced LCS intersect the landing trajectory and appear to have an impact on the approaches.

In Figs. 8c,d, we compare LCS with onboard data. The most important onboard data relevant to our analysis are the measured vertical accelerations of aircraft during the landings as they measure the response to the aircraft to aerial disturbance. In the absence of any disturbance, the perturbed vertical acceleration of the plane is zero, resulting in a constant speed of descent. The vertical acceleration data are given in units of gravitational constant g (9.81 m s^{-2}). Therefore, acceleration values above (below) $0g$ indicate updrafts (downdrafts).

Because the aircraft measures data at higher frequency as compared with lidar, small-scale variations make a direct comparison between LCS and vertical acceleration challenging. We thus require net acceleration to be larger than $0.05g$ to qualify as significant air disturbances. More detailed explanation for this threshold is given later in the section. In Figs. 8c,d, net acceleration is plotted as the black curve, in units of g . Note that we only plot the relevant structures in the acceleration data, that is, downdrafts only in Fig. 8c and updrafts only in Fig. 8d, with values less than the threshold set to 0. This helps visual comparison among datasets. The two black dashed lines in Figs. 8c,d show references of $\pm 0.05g$.

To compare these air disturbances with LCS, we interpolate the FDFTLT and DIV fields along the landing trajectory at times when the airplane reaches the same locations (thus the interpolation is based on a time

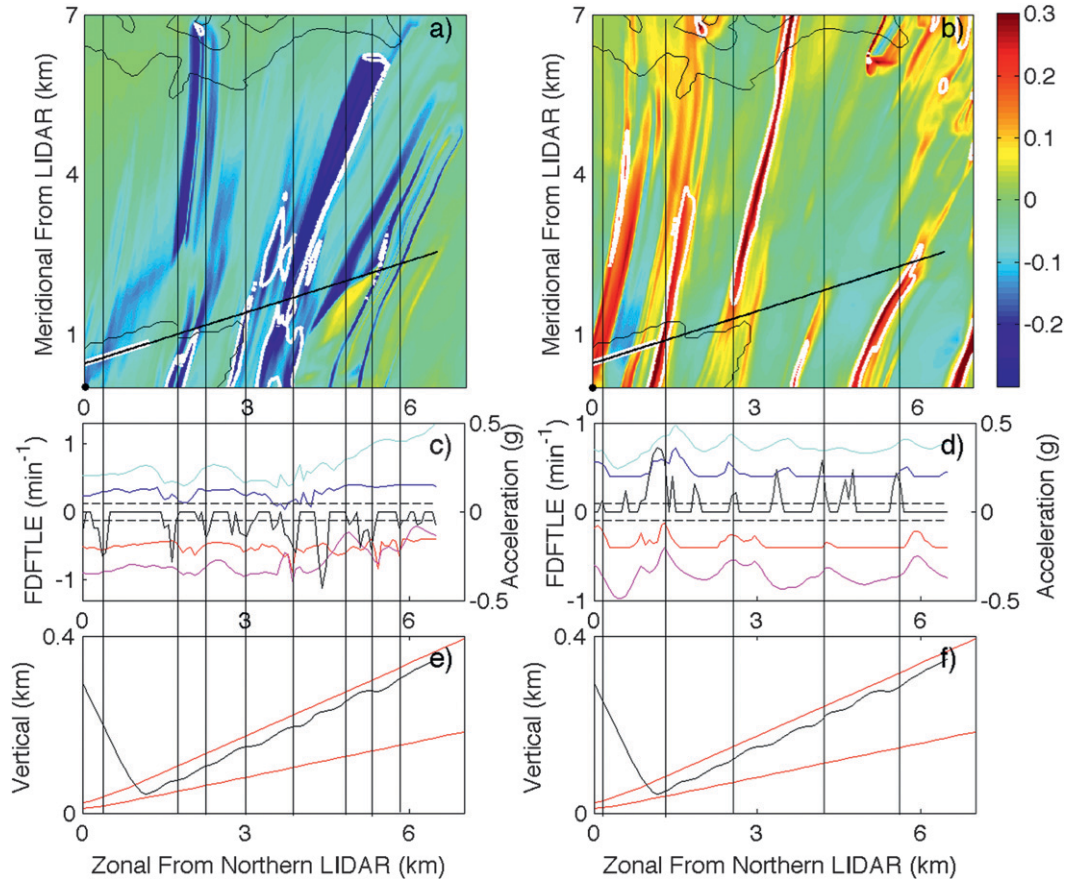


FIG. 8. Airplane-landing data in comparison with LCS for missed approach at 1346 UTC 19 Apr 2008. (a) Approach superimposed on forward-time FDFMLE based on the 1.4° scan. The black isocontours indicate terrain near HKIA. The thick white line in the lower-left corner denotes the northern runway. The thin black line along the runway denotes approaching trajectory. The black dot at (0, 0) indicates the position of the northern lidar. White isocontours are DIV = -0.12. (b) Approach superimposed on backward-time FDFMLE. White isocontours are DIV = 0.09. All else is as in (a). (c) Comparison between negative vertical acceleration and forward-time FDFMLE. Vertical acceleration measured on board the aircraft is shown in black, with values > -0.05g removed, along with references of -0.05g and 0.05g, plotted in dashed lines. The blue (red) solid lines are the FDFMLE generated from the 3.0° (1.4°) scans and shifted by ±0.4. The cyan (magenta) solid lines are the DIV generated from the 3.0° (1.4°) scans and shifted by ±0.8. For ease of comparison, negative values of FDFMLE and DIV are plotted. (d) Comparison between backward-time FDFMLE and vertical acceleration as in (c). (e),(f) The airplane altitude as it approaches the runway (black line), along with the 3.0° and 1.4° scan cones (red lines). The black vertical lines highlight places where LCS are correlated with vertical acceleration.

evolution of the LCS). For example, in Fig. 8c, for ease of comparison between downdrafts and LCS, we plot negative values of the forward-time FDFMLE and DIV interpolation, so downdrafts can be directly compared with troughs of FDFMLE-DIV. Since the airplane landing is usually between the 1.4° and 3.0° lidar cones, we show interpolations along the landing trajectory based on both elevation angles. The red curves in Figs. 8c,d are FDFMLE based on 1.4° scans and the blue curves are FDFMLE based on 3.0° scans. For clarity, we have shifted the red curves by -0.4 and blue curves by 0.4. Similarly, the magenta curves are DIV based on 1.4° scans

shifted by -0.8 and the cyan curves are DIV based on 3.0° scans shifted by 0.8. The peak-peak and trough-trough correspondence indicate correlation of LCS and air disturbances.

In Figs. 8e and 8f, we show comparisons between lidar scan cones and the airplane altitude as it approaches the runway. Since the runway corridor is generally between the two lidar cones (until the airplane touches down, when it descends below the 1.4° scan), locations of the aircraft relevant to the lidar cones indicate which scan is more reliable. The two lidar cones are shown in red, along with the airplane altitude in black. For this

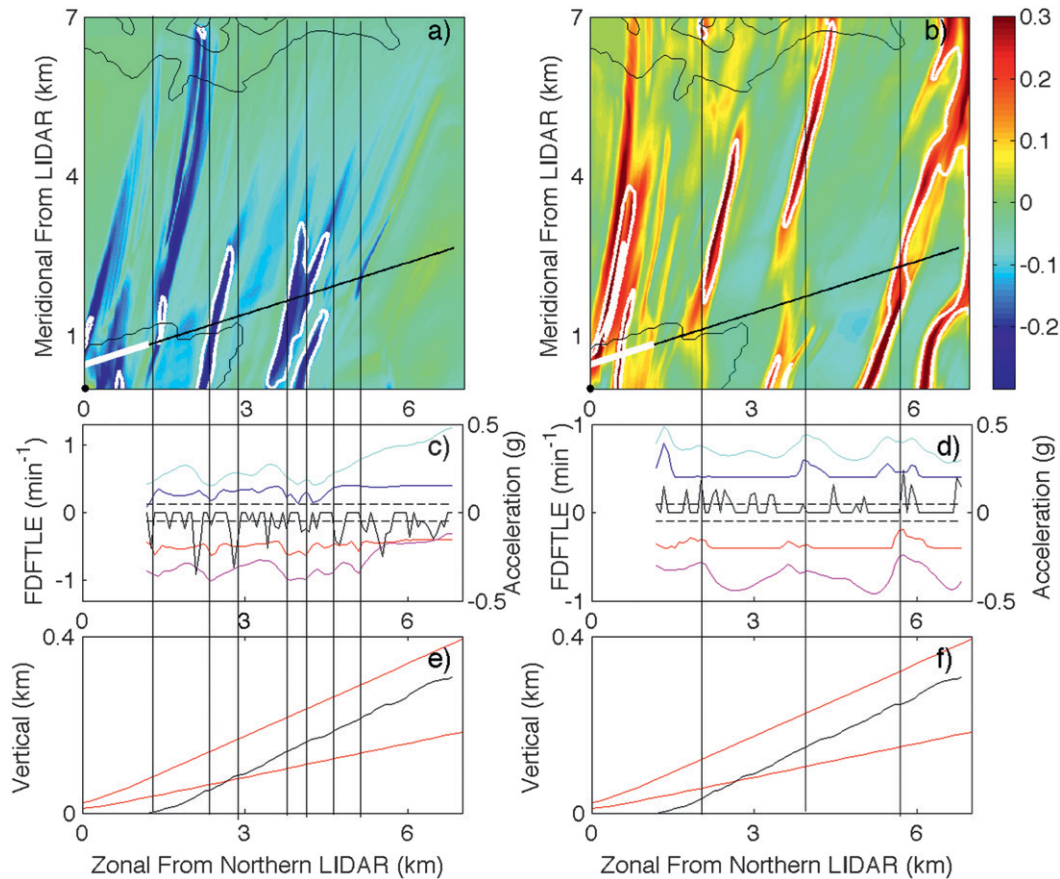


FIG. 9. Airplane-landing data in comparison with LCS for successful approach at 1414 UTC 19 Apr 2008. Plot layout is as in Fig. 8. Note that the persistent ridge of updraft downwind of Lin Fa Shan discussed in section 3 does affect both landings.

approach, the airplane decreases altitude toward the runway threshold at about 1 km (0 km is the location of the northern lidar). At the runway threshold the airplane is still quite high, and it also experiences an updraft. The airplane is pulled up to conduct its second approach. The vertical acceleration profile and the dipping/flattening patterns in its altitude suggest that the aircraft indeed experiences several updrafts.

To aid comparison, we use black vertical lines to align air disturbances that are correlated to LCS. For example, in Fig. 8c, we first locate troughs of (negative) forward-time FDFTLE. Near these troughs, especially the significant ones, we observe strong downdrafts. We draw vertical lines when such correspondences exist and extend them to the top and bottom panels. It is seen that in Figs. 8a and 8b the vertical lines can be associated with airplane trajectories intersecting with the FDFTLE ridges. In Figs. 8e and 8f these reference lines can also be associated with several disturbances to the airplane descending trajectories. We do not require a precise match

in location since the lidar scans and onboard measures are independent sets of data and do not match precisely. Henceforth, as long as the FDFTLE extrema and the significant air disturbances are fairly close by (we provide explanation later), we claim that there is a match between the two peaks/troughs. It is seen in Fig. 8, especially in Figs. 8c and 8d, that almost all FDFTLE extrema can be associated with significant air disturbances. *The reverse argument is not true as airplane data have higher frequencies and thus have more variations than LCS.*

Figure 9 depicts the successful approach of the same flight at 1414 UTC, where we find again correspondence in location of the FDFTLE/DIV extrema and some significant air disturbances. It is interesting to confirm that the ridge of updraft that originated from Lin Fa Shan, as discussed in section 3, plays an important role as time progresses and that it affects both approaches of the same flight. The recirculation structure trailing Cheung Shan and its shedding generation appears to be toward the farther end of the runway for airplane landings.

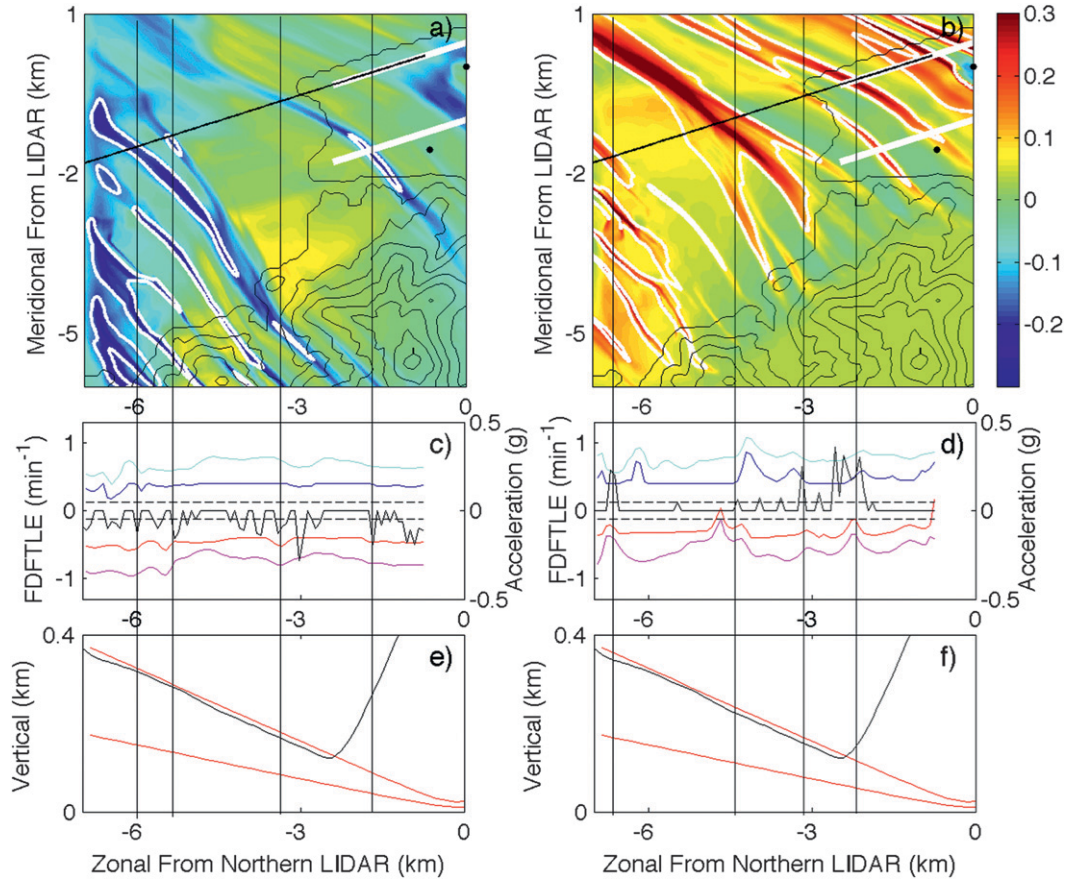


FIG. 10. Airplane-landing data in comparison with LCS for missed approach at 0837 UTC 21 Feb 2009. Plot layout is as in Fig. 8 except that the range is focused on the landing trajectory to the west of the northern lidar. The southern lidar is also plotted in the figure for reference.

For the February 2009 case, the missed and successful approaches are from the west, as depicted in Figs. 10 and 11. Both runways and lidars are visible in these figures. The number of FDFTLTLE extrema is less than the April 2008 case, probably because of the runway threshold being closer to the boundary of the domain. However, we see correspondence between the few peaks and troughs and the several significant updrafts and downdrafts. For the backward-time FDFTLTLE in both approaches, we find that the few persistent ridges are associated with several updrafts close to or exceeding the threshold for significant air disturbances. On the basis of this and data from April 2008 landings, we suspect that the existence of persistent ridges in stable boundary layers of cyclones is of concern for aircraft approaches. More analyses of similar synoptic cases are needed to confirm such a relationship.

To further elaborate on the correspondence between the locations of LCS and air disturbances experienced on board the aircraft, we use the following measures to compute their correlations. For each FDFTLTLE/DIV

extremum, we search for a corresponding significant air disturbance (i.e., a jolt experienced by the plane) within a 150-m radius of the LCS.

By a *jolt*, we will mean a disturbance that results in a lift force on the aircraft that differs from the weight of the plane by more than 5%. Specifically, a jolt occurs at time t if

$$\text{onboard vertical acceleration at time } t \text{ is } > 0.05g. \quad (5)$$

If such a jolt can be found within 150 m from an LCS crossed by the flight path, we assign the value of 1 to this crossing to signify the correspondence between the pair; otherwise we assign 0 to signify no correspondence. The average of these values over all observed LCS crossing flight paths provides an empirical estimate for the conditional probability

$$p_{\text{LCS} \rightarrow \text{jolt}} = P(\text{jolt observed within 150 m of LCS} | \text{LCS found on flight path}), \quad (6)$$

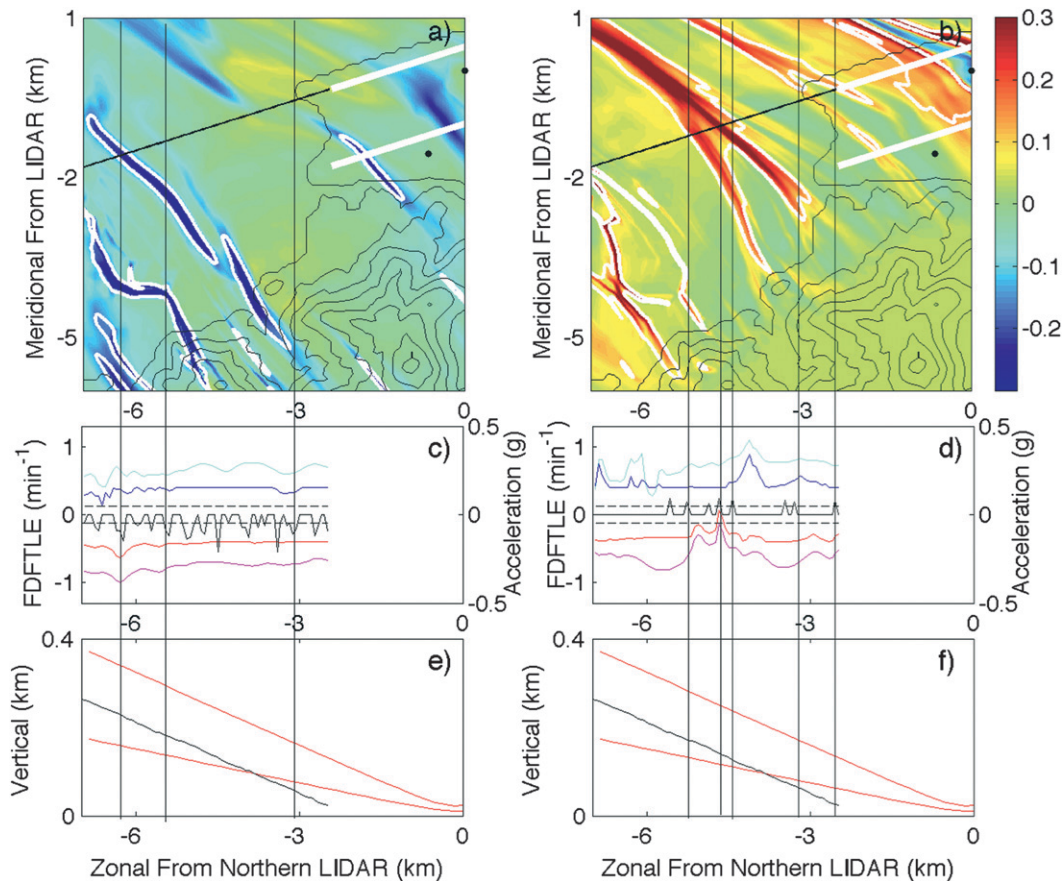


FIG. 11. Airplane-landing data in comparison with LCS for successful approach at 0902 UTC 21 Feb 2009. Plot layout is as in Fig. 8 except that the range is focused on the landing trajectory to the west of the northern lidar. The southern lidar is also plotted in the figure for reference. In these two landings, large-scale updraft structures also correspond well to the vertical accelerations measured on board.

which measures the reliability of LCS detection in predicting jolts.

Similarly, for every significant air disturbance along the flight path, we may search for an LCS crossing the flight path within a 150-m radius. We again assign 1 to the outcome of this search if such an LCS is found and assign 0 if no such LCS is found. Again, the average of all these 1s and 0s will provide an empirical estimate for the conditional probability

$$p_{\text{jolt} \rightarrow \text{LCS}} = P(\text{LCS found on flight path within } 150 \text{ m of jolt} | \text{jolt observed}), \quad (7)$$

which measures the probability that the FDFTLTLE has a signature near every single jolt. Note that $p_{\text{LCS} \rightarrow \text{jolt}}$ enhances the correlation effects in terms of the locations of jolts and LCS.

The 150-m threshold in the above definitions arises from the following consideration. Low-level turbulence,

for aviation purposes, is typically considered to have a time scale that is below 3 s. We would, therefore, consider an LCS prediction to be timely if it is no more than 2 s apart from a jolt experienced on board the aircraft. Since the speed of a landing aircraft is around $75\text{--}100 \text{ m s}^{-1}$, the plane covers a distance of at least 150 m in 2 s, motivating the use of the spatial scale in the definitions given by Eqs. (6) and (7).

We illustrate in Fig. 12 the generation of conditional probability measures described above. The case shown is for the missed approach at 1346 UTC 19 April 2008. In Figs. 12a,b, we show again the direct peak/trough comparison among vertical acceleration measured on board, FDFTLTLE and DIV for forward-time and backward-time structures. These plots are the same as Figs. 8c,d. Since the confidence of LCS is more on the geometric locations of updrafts/downdrafts rather than on the magnitudes, we normalize the strength of the peaks/troughs of vertical acceleration, FDFTLTLE and DIV. This is seen in Figs. 12c,d. We then conduct a search for each

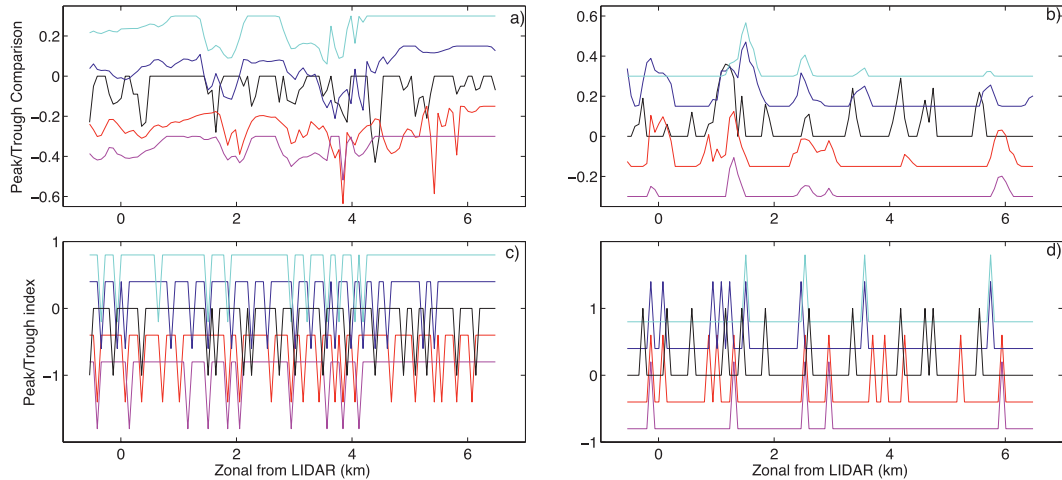


FIG. 12. Development of the conditional probability. The example shown is for the missed approach at 1346 UTC 19 Apr 2008. (a) Comparisons among negative vertical acceleration and forward-time FDFTL/DIV. Black: downdrafts measured on board. Red: FDFTL at 1.4°. Magenta: DIV at 1.4°. Blue: FDFTL at 3.0°. Cyan: DIV at 3.0°. (b) Layout as in (a), but for backward-time integration [(a) and (b) are essentially the same as Figs. 8c and 8d]. (c) The troughs are normalized to 1 and correlation is searched if a downdraft is within 150 m of an FDFTL/DIV trough. (d) As in (c), but for updrafts and peaks in backward-time measures.

FDFTL/DIV extremum and look for extrema of vertical acceleration within 150 m. This forms the measures $p_{\text{FDFTL} \rightarrow \text{jolt}}$ and $p_{\text{DIV} \rightarrow \text{jolt}}$. Conversely, for each extremum of vertical acceleration, we conduct a search for nearby FDFTL/DIV extrema, which forms the measures $p_{\text{jolt} \rightarrow \text{FDFTL}}$ and $p_{\text{jolt} \rightarrow \text{DIV}}$. It is difficult to do any higher-resolution comparison because the Lagrangian measures are derived from spatial (100-m range gate) and temporal (~ 20 s per PPI scan) averages and hence are unlikely to produce spatial structures exactly matching onboard measurements. We note that the conditional probability $p_{\text{LCS} \rightarrow \text{jolt}}$ is likely to take high values, since as long as the (few) peaks/troughs are near an updraft/downdraft, this correlation can be very high. In the example shown, we obtain the probabilities as listed in Table 1. Consider, for instance, the backward-time measures. Six out of 10 peaks in the red curve in Fig. 12d correlate well in position with some peaks in the black curve. Conversely, 6 out of 12 peaks in the black curve correlate with the peaks in the red curve. This leads to $p_{\text{FDFTL} \rightarrow \text{jolt}} = 0.6$ and $p_{\text{jolt} \rightarrow \text{FDFTL}} = 0.5$.

Evaluating the 20 landing cases at hand, we find that the probabilities measuring the efficacy of jolt forecasting via FDFTL/DIV are as listed in Table 2. Standard deviations in each of the measurements are also shown. Note that the measure for individual cases may be quite different from the averages, as seen by contrasting values in Tables 1 and 2.

Recall that LCS corresponding to downdrafts are obtained from forward-time analysis and hence are based on present and future data. By contrast, LCS corresponding

to downdrafts are obtained from backward-time analysis, which only use data available up to the present time. The use of future data appears responsible for the higher accuracy in downdraft detection, as seen in the first two columns of Table 2. That said, updraft detection via LCS (last two columns of Table 2) still yields detection probabilities over 0.5 in most cases, except for $p_{\text{jolt} \rightarrow \text{DIV}}$. The low values of $p_{\text{jolt} \rightarrow \text{DIV}}$ could be the result of lidar cones approaching higher altitude when farther away from the lidar, and hence the near-ground effects on horizontal divergence are not easily visible (cf. Fig. 12). In all panels, the DIV curves 4 km away from the lidar do not bear many structures correlating with the onboard measurements, except for one updraft at 6 km, which was probably due to a very strong vertical motion.

Considering that (i) the quality of wind shear measurement (and hence of jolt detection) on commercial aircraft is limited and does not reach the quality provided by fixed-wing research aircraft, (ii) jolt detection and LCS extraction typically take place at different altitudes and hence vertical deformation is likely to be a

TABLE 1. Correlation between jolts and LCS at 1346 UTC 19 Apr 2008.

	LCS downdrafts		LCS updrafts	
	1.4° scan	3.0° scan	1.4° scan	3.0° scan
$p_{\text{FDFTL} \rightarrow \text{jolt}}$	0.6667	0.6667	0.6	0.5455
$p_{\text{jolt} \rightarrow \text{FDFTL}}$	0.6667	0.7222	0.5	0.4167
$p_{\text{DIV} \rightarrow \text{jolt}}$	0.6364	0.5833	0.5	0.4
$p_{\text{jolt} \rightarrow \text{DIV}}$	0.4444	0.3889	0.3333	0.1667

TABLE 2. Correlation between jolts and LCS for 20 cases.

	LCS downdrafts		LCS updrafts	
	1.4° scan (std dev)	3.0° scan (std dev)	1.4° scan (std dev)	3.0° scan (std dev)
$P_{\text{FDFTLE} \rightarrow \text{jolt}}$	0.8066 (0.1633)	0.7477 (0.1745)	0.6214 (0.2305)	0.6204 (0.211)
$P_{\text{jolt} \rightarrow \text{FDFTLE}}$	0.6928 (0.1012)	0.6805 (0.0882)	0.5280 (0.1921)	0.5415 (0.1491)
$P_{\text{DIV} \rightarrow \text{jolt}}$	0.7643 (0.1888)	0.7615 (0.1615)	0.5819 (0.2265)	0.5700 (0.2714)
$P_{\text{jolt} \rightarrow \text{DIV}}$	0.3872 (0.1057)	0.3837 (0.1195)	0.3480 (0.1618)	0.3103 (0.1511)

significant factor for the correlation, and (iii) Lagrangian measures are based on PPI scans, which take heavy spatial and temporal averaging (as compared with the resolution of onboard measurements), we conclude that, on the basis of available 2D lidar data, Tables 1 and 2 provide compelling support for the applicability of LCS analysis in real-time aerial turbulence detection over commercial airports.

5. Conclusions and discussion

We have used Lagrangian tools developed in Tang et al. (2010, 2011) to study the evolution of aerial coherent structures near HKIA and to assess the efficacy of LCS analysis in real-time aerial turbulence detection.

We extracted LCS from two synoptic flow cases between April 2008 and February 2009 at consecutive time intervals of 150 s, the update rate of the lidar outputs. Among these LCS, we have found structure generation and shedding from patches of velocity anomalies aloft of mountain peaks and ridges. Also, large-scale LCS associated with updraft appear to be created by the topography of Lin Fa Shan, south of the airport. A real-time detection of these LCS is expected to provide crucial information for aviation hazard detection.

To assess the feasibility of using LCS in a real-time turbulence alert system, we compared available onboard landing data with the LCS extracted from lidar observations on the ground. We have found compelling evidence (cf. Tables 1 and 2) that locations of LCS (detected as ridges of the FDFTLE field) and significant air disturbances (indicated by onboard measurements of the plane's vertical acceleration exceeding 0.05g) are correlated. The detection probability values in Table 2 are especially promising if one recalls that the lidar cone used in this analysis has typically only one intersection of the flight part of the plane. As a result, we compare LCS and vertical acceleration mostly at different altitudes, and hence our analysis does not yet account for the vertical deformation of LCS with varying altitude. This is a crucial drawback, as the operational algorithm at HKIA uses scans exactly on the flight path (Chan et al. 2006) and has better performance than the current Lagrangian algorithm. The use of information precisely on the flight path may lead to

significant improvements to the technique, but it cannot be achieved by the PPI scans since the glide path has varying PPI angle. Existing glide path scans cannot be used for Lagrangian analyses either since they are limited in the azimuthal angles. This calls for better comparisons/schemes for the operational use of our algorithm.

Recently, the Hong Kong Observatory has completed the installation of meteorological equipment on a fixed-wing aircraft. This will provide higher-quality aircraft data as compared with data from commercial jets and is expected to result in a further increase in the correlation between jolts on the aircraft and LCS observed from lidars.

Moreover, as pointed out in Tang et al. (2011), there is a technical challenge in extracting repelling LCS (Lagrangian downdrafts) from forward-time FDFTLE for operational use, because lidar scans are nowcasts. For two-dimensional flows, Haller and Iacono (2003) provide a method for extracting attracting and repelling LCS from a single, unidirectional integration of trajectories. We are testing this approach in the hope of removing dependencies on measurements not yet available, which cannot be built into an operational algorithm.

A further improvement in our ability to predict jolts from LCS will be aided by the recent availability of three-dimensional time-resolved (4DVAR) wind field data. Three-dimensionality of data will address the altitude mismatch between extracted LCS and measured vertical acceleration along the flight part and, as mentioned earlier, may lead to significant improvements of our algorithm. Currently, we are analyzing 4DVAR data for the April 2008 case. Note that the above approaches are still bounded by the accuracy of lidar measurements and quality of retrieval techniques.

Alternatively, we are conducting high-resolution simulations of regional climate models for the cases of interest and performing Lagrangian analyses on these datasets. We also consider assimilating lidar data in the regional models for short-term [$\sim(10\text{--}20)$ min] forecasts. The validity of Lagrangian approaches will be further tested there and it is hoped that with improved quality of the velocity datasets we will be closer to the operational use of Lagrangian tools in airflow hazard detection near airports. All these challenges will be explored in future publications.

Acknowledgments. We thank Cathay Pacific Airways for the supply of flight data with agreement of the Hong Kong Aircrew Officers Association (HKAOA). We thank three anonymous referees for their careful reading and helpful inputs. Author WT also acknowledges support from the National Science Foundation (ATM-0934592); GH was partially supported by AFOSR Grant FA9550-06-1-0092.

REFERENCES

- Atkinson, B. W., 1981: *Meso-Scale Atmospheric Circulations*. Academic Press, 495 pp.
- Chan, P. W., and C. M. Shun, 2005: Numerical simulation of vortex shedding observed at the Hong Kong International Airport using a shallow water model. *Croat. Meteor. J.*, **40**, 27–30.
- , and A. M. Shao, 2007: Depiction of complex airflow near Hong Kong International Airport using a Doppler LIDAR with a two-dimensional wind retrieval technique. *Meteor. Z.*, **16**, 491–504.
- , C. M. Shun, and K. C. Wu, 2006: Operational lidar-based system for automatic wind shear alerting at the Hong Kong international airport. Preprints, *12th Conf. on Aviation, Range, and Aerospace Meteorology*, Atlanta, GA, Amer. Meteor. Soc., 6.11. [Available online at http://ams.confex.com/ams/Annual2006/techprogram/paper_100601.htm.]
- Haller, G., 2001: Distinguished material surfaces and coherent structures in three-dimensional fluid flows. *Physica D*, **149**, 248–277.
- , 2011: A variational theory of hyperbolic Lagrangian coherent structures. *Physica D*, **240**, 574–598.
- , and G. Yuan, 2000: Lagrangian coherent structures and mixing in two-dimensional turbulence. *Physica D*, **147**, 352–370.
- , and R. Iacono, 2003: Stretching, alignment, and shear in slowly varying velocity fields. *Phys. Rev. E*, **68**, doi:10.1103/PhysRevE.68.056304.
- Mathur, M., G. Haller, T. Peacock, J. E. Ruppert-Felsot, and H. L. Swinney, 2007: Uncovering the Lagrangian skeleton of turbulence. *Phys. Rev. Lett.*, **98**, doi:10.1103/PhysRevLett.98.144502.
- Shadden, S. C., F. Lekien, and J. E. Marsden, 2005: Definition and properties of Lagrangian coherent structures from finite-time Lyapunov exponents in two-dimensional aperiodic flows. *Physica D*, **212**, 271–304.
- Shun, C. M., S. Y. Lau, and O. S. M. Lee, 2003: Terminal Doppler weather radar observation of atmospheric flow over complex terrain during tropical cyclone passages. *J. Appl. Meteor.*, **42**, 1697–1710.
- Tang, W., P. W. Chan, and G. Haller, 2010: Accurate extraction of Lagrangian coherent structures over finite domains with application to flight data analysis over Hong Kong International Airport. *Chaos*, **20**, 017502, doi:10.1063/1.3276061.
- , —, and —, 2011: Lagrangian coherent structure analysis of terminal winds detected by lidar. Part I: Turbulence structures. *J. Appl. Meteor. Climatol.*, **50**, 325–338.
- Toth, Z., and E. Kalnay, 1997: Ensemble forecasting at NCEP and the breeding method. *Mon. Wea. Rev.*, **125**, 3297–3319.